

# Controlled symmetry breaking and vortex dynamics in intersecting flows F

Cite as: Phys. Fluids **31**, 034104 (2019); <https://doi.org/10.1063/1.5087732>

Submitted: 03 January 2019 . Accepted: 13 February 2019 . Published Online: 07 March 2019

Noa Burshtein , Amy Q. Shen , and Simon J. Haward 

## COLLECTIONS

F This paper was selected as Featured



View Online



Export Citation



CrossMark

## ARTICLES YOU MAY BE INTERESTED IN

[Linear analysis of non-local physics in homogeneous turbulent flows](#)

Physics of Fluids **31**, 035102 (2019); <https://doi.org/10.1063/1.5085239>

[Boundary integral simulations of a red blood cell squeezing through a submicron slit under prescribed inlet and outlet pressures](#)

Physics of Fluids **31**, 031902 (2019); <https://doi.org/10.1063/1.5081057>

[Is Tollmien-Schlichting wave necessary for transition of zero pressure gradient boundary layer flow?](#)

Physics of Fluids **31**, 031701 (2019); <https://doi.org/10.1063/1.5089294>



CAPTURE WHAT'S POSSIBLE  
WITH OUR NEW PUBLISHING ACADEMY RESOURCES

Learn more 





# Controlled symmetry breaking and vortex dynamics in intersecting flows

Cite as: Phys. Fluids 31, 034104 (2019); doi: 10.1063/1.5087732

Submitted: 3 January 2019 • Accepted: 13 February 2019 •

Published Online: 7 March 2019



View Online



Export Citation



CrossMark

Noa Burshtein,  Amy Q. Shen,  and Simon J. Haward<sup>a)</sup> 

## AFFILIATIONS

Okinawa Institute of Science and Technology, Onna, Okinawa 904-0495, Japan

<sup>a)</sup>Electronic mail: [simon.haward@oist.jp](mailto:simon.haward@oist.jp)

## ABSTRACT

Vortices are a ubiquitous feature in complex flows and turbulence, but their dynamics are challenging to study due to their typically transient nature. Here, we perform a detailed study of the vortex dynamics and interactions associated with a symmetry-breaking flow instability at a 4-way intersection. By precisely controlling the flow rate (hence the Reynolds number,  $Re$ ) of the flow about a critical value, we are able to induce the merging of two co-rotating vortices into a single structure and similarly to induce a single vortex to split into two. Using quantitative flow velocimetry, both processes are recorded with high spatial and temporal resolution. We find that both the merging and the splitting of vortices are exponential processes, with a rate that depends on the imposed  $Re$ . The vortex dynamics in our system are intimately connected with the symmetry-breaking transition and are affected by the degree of vortex confinement, which we control by varying the aspect ratio ( $\alpha$ ) of the flow geometry. We show how the confinement affects the fundamental nature of the flow transition, which varies from super through subcritical as  $\alpha$  is increased. Our results are of direct relevance to understanding and predicting flow transitions and vortex dynamics in flow intersections, particularly in confined environments such as in microfluidic (lab-on-a-chip) devices and in the circulatory system, and may be relevant to the prediction of vortex interactions in general.

© 2019 Author(s). All article content, except where otherwise noted, is licensed under a Creative Commons Attribution (CC BY) license (<http://creativecommons.org/licenses/by/4.0/>). <https://doi.org/10.1063/1.5087732>

## I. INTRODUCTION

Swirling flows and formation of vortices have been attracting scientific attention for centuries due to their intriguing nature and prevalence in diverse environments. Vortices frequently occur in geophysical flows, where they may lead to turbulence resulting in violent storms such as tornados and hurricanes.<sup>1</sup> The continuous merging and splitting of the vortices in the upper levels of the atmosphere above the poles influence the weather around the globe.<sup>2-4</sup> Vortices are crucial in many industrial and engineering applications. In particular, the formation of trailing vortices in the wake of airplanes may cause unpredictable turbulent flow and require redirection of following air traffic.<sup>5,6</sup> Vortices are also formed by the movement of winged creatures and are an important feature in their flight.<sup>7</sup> Even in relatively viscous flows such as in pipes and channels with small length scales, vortices can play a significant role in the fluid dynamics, particularly at

flow intersections such as T-, Y-, and X-junctions or around bends.<sup>8-17</sup> Such configurations are common features in all flow loops including biological circulation systems. Additionally, vortices are commonly generated in inviscid environments such as superfluids and electro-magnetic fields. The dynamics of these vortices resembles two dimensional ideal flows,<sup>18-20</sup> and they are often analyzed with classical fluid dynamics tools.<sup>21,22</sup>

Vortices are especially important in the study of turbulent flows and can be regarded as their building blocks, as they may form more defined (coherent) structures which contain most of the kinetic energy in the flow.<sup>23,24</sup> Vortex merging and splitting are at the heart of the energy cascade of turbulent flows.<sup>25-27</sup>

The merging process of two co-rotating vortices has been broadly studied due to its practical importance to aircraft trailing vortices. Experimental apparatus and numerical models that recreate trailing vortices enable the mechanism of the

merging process to be studied in detail and have been discussed in several studies.<sup>28–36</sup> Although there is still an ongoing debate about how to define a vortex,<sup>37,38</sup> there is a general agreement that the mechanism of merging consists of three main stages: (1) the first diffusive stage in which the core of each vortex grows, (2) the convective stage, in which the vortices rapidly move towards one another, and (3) the second diffusive stage in which the vortices have merged into a single structure.<sup>35,36,39,40</sup>

In contrast to vortex merging, the process of vortex splitting is much more challenging to induce and study, and experimental evidence of the phenomenon is scarce.<sup>41–44</sup>

In this study, we achieve well-controlled inducement of both vortex merging and splitting by employing a canonical extensional flow device. The device, known as a “cross-slot” geometry, consists of a 4-way flow intersection with two oppositely facing inlets and two oppositely facing outlets, see Figs. 1(a) and 1(b) (Multimedia view). At low values of the dimensionless flow velocity (or Reynolds number,  $Re$ ), the flow along the outlet channels is symmetric about  $y$  and  $z$  and comprises of four cells of Dean vortices, Fig. 1(c) (Multimedia view). However, if  $Re$  is increased beyond a critical value  $Re_c$ , the flow breaks symmetry and one pair of co-rotating Dean vortices approach each other and merge to form a single steady streamwise stretched vortex (similar to a Burgers vortex),<sup>45,46</sup> centrally aligned along the outlet channel, Figs. 1(d) and 1(e)

(Multimedia view). By a reduction in Reynolds number from an initial value  $Re > Re_c$ , the opposite process can be observed in which a single vortex splits into two co-rotating vortices that migrate away from each other as the flow regains symmetry [Figs. 1(c)–1(e) (Multimedia view)]. The processes can be directly visualized on a microscope, and the streamwise vorticity can be quantitatively measured using time-resolved flow velocimetry [Fig. 1 (Multimedia view)].<sup>14</sup>

In our experimental system, the Dean vortices are each confined within a quadrant of the channel cross section dictated by the boundaries of the channel and by the neighboring counter-rotating vortices. As a result, complications arising from the Fujiwhara effect are eliminated and we avoid the need to employ a rotating reference frame in our analyses.<sup>38,47,48</sup> We perform experiments by controlling  $Re$  in two distinct ways: (1) increasing and decreasing quasistatic ramps of  $Re$  in which the flow is observed under steady conditions at each  $Re$  increment and (2) large step increases or decreases in  $Re$  in which the flow is observed as it dynamically approaches the steady state at above or below  $Re_c$ . While the origin of symmetry breaking has previously been linked to vortex dynamics through numerical studies of the vortex shedding downstream of a circular cylinder,<sup>49</sup> our work represents the first time that the relationship between symmetry breaking and the merging and splitting of vortices has been studied under such controlled experimental conditions. In addition, we examine the effect of varying the aspect ratio of the rectangular inlet and outlet channels [ $\alpha = d/w$ , where  $d$  and  $w$  are the channel depth and width, respectively, Fig. 1(b) (Multimedia view)]. A previous study has shown that the symmetry-breaking flow bifurcation changes from supercritical (non-hysteretic) for low  $\alpha \lesssim 0.55$  to subcritical (i.e., hysteretic) for  $\alpha \gtrsim 0.55$  (with a tricritical transition occurring for  $\alpha \approx 0.55$ ).<sup>13</sup> Here we report how the vortex dynamics depends intimately on the nature of the flow transition.

Our observations and measurements show that changing  $\alpha$  affects the degree to which the Dean vortices are confined within their respective quadrants of the channel cross section (lower  $\alpha$  implies greater confinement). This modifies the relative rates of merging and splitting as  $Re$  is increased or decreased (respectively) past the critical point, providing a rationalization for the emergence of hysteresis in the system at higher values of  $\alpha$ .

Our experimental methods provide a new approach to the study of vortex dynamics, in particular vortex splitting, in an extremely well-controlled experimental frame. Our findings suggest that the physical mechanisms underlying vortex merging and splitting can be affected by the confinement of the vortices and we identify possible changes in the mechanisms that govern these widespread and important processes.

## II. MATERIALS AND METHODS

### A. Microfluidic devices

Four microfluidic cross-slot channels with different values of the aspect ratio  $\alpha$  are fabricated in fused silica by selective laser-induced etching using a “LightFab” 3D printer

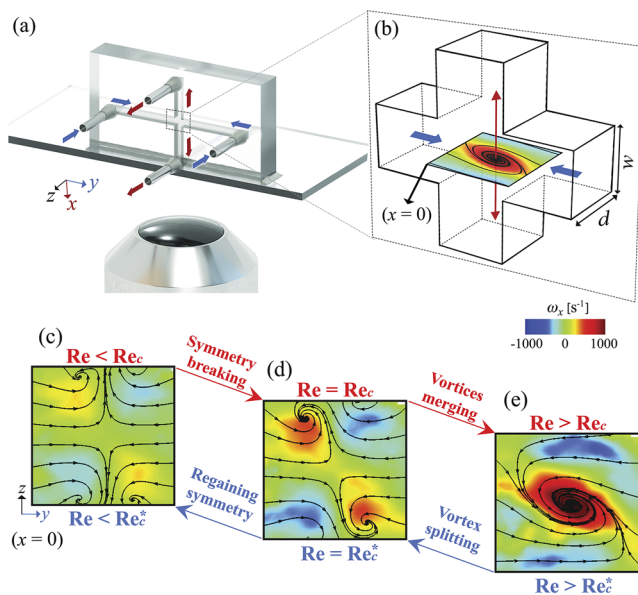


**FIG. 1.** (a) A schematic diagram of the experimental setup, which allows a direct observation of the  $x = 0$  plane on an inverted microscope. Inflow (along  $y$ ) is indicated by the blue arrows, and outflow (along  $x$ ) is indicated by the red arrows. (b) Schematic diagram of a vortex in the cross-slot device for flow at  $Re > Re_c$ ;  $d$  and  $w$  are the channel depth and width, respectively. [(c)–(e)]  $\mu$ -PIV images of the vorticity field at  $x = 0$ : (c) a symmetric flow field with four cells of Dean vortices; (d) an asymmetric flow field where two intensified Dean vortices have commenced to merge; and (e) a single steady, central streamwise vortex is formed by the merging of the two Dean vortices. Multimedia view: <https://doi.org/10.1063/1.5087732.1>

TABLE I. Specifications of the microfluidic cross-slot devices.

$\alpha$	$w$ ( $\mu\text{m}$ )	$d$ ( $\mu\text{m}$ )	Transition type	$Re_c$	$Re_c^*$
0.45	1490	670	Supercritical	107.5	107.5
0.57	1460	830	Near tricritical	76.0	75.0
1.1	990	1060	Subcritical	40.2	36.5
2.4	620	1500	Subcritical	26.5	21.4

(LightFab GmbH, Germany).<sup>50–52</sup> The chosen aspect ratios capture both supercritical ( $\alpha \lesssim 0.55$ ) and subcritical (hysteretic,  $\alpha \gtrsim 0.55$ ) flow transitions, see Table I.<sup>13</sup> By measurement of the channel dimensions subsequent to fabrication, the error in quoted values of  $\alpha$  is estimated to be  $\pm 1\%$ .

The device inlet lengths are set to be 16 mm, giving a high ratio ( $>10$ ) between the inlet length and the largest channel dimension, ensuring fully developed flow before the fluid reaches the 4-way intersection of the cross-slot. The outlets are designed to be as long as possible ( $\approx 5$  mm), while still allowing imaging to be performed at the  $yz$  centerplane [at  $x = 0$ , see Fig. 1(b) (Multimedia view)].

The inlets and outlets are connected to four individually controlled high precision neMESYS syringe pumps (Cetoni GmbH, Germany) fitted with Hamilton Gastight syringes. Two of the pumps drive fluid into the two opposed inlets, while the other two pumps withdraw fluid simultaneously from the two outlets of the device (all at equal volumetric flow rates). The pumps are operated at a minimum of  $10\times$  (and typically  $>50\times$ ) the manufacturer's specified lowest "pulsation-free" dosing rate. In order to keep the system compliance at a minimum, the tubing between the syringes and the device is made of rigid poly(tetrafluoroethylene), the tubing is kept as short as possible, and great care is taken to purge all air from the system.

The transition from symmetric to asymmetric flow is directly controlled by the magnitude of the Reynolds number, which describes the ratio of inertial to viscous forces in the flow,

$$Re = \frac{Uw}{\nu}, \quad (1)$$

where  $U$  is the average flow velocity in each channel of the cross-slot device. All of our experiments involve the flow of deionized water with a kinematic viscosity  $\nu = 8.9 \times 10^{-7} \text{ m}^2 \text{ s}^{-1}$  at  $25^\circ\text{C}$ . All experiments are carried out at  $25 \pm 1^\circ\text{C}$ , and the estimated error in  $Re$  is around  $\pm 1\%$ .

As described in the Introduction, for low values of  $Re$  the flow field is symmetric and stable, as demonstrated in Fig. 1(c) (Multimedia view). If  $Re$  is increased beyond the critical value  $Re_c$ , the symmetry breaks and the process of vortex merging proceeds [Figs. 1(d) and 1(e) (Multimedia view)]. When performing the opposite experiment (reducing  $Re$  from an initial value  $>Re_c$ ), the central vortex will split into two co-rotating vortices and the flow field will regain symmetry at  $Re < Re_c^*$ . For supercritical transitions  $Re_c = Re_c^*$ , but for subcritical transitions  $Re_c > Re_c^*$  due to the hysteresis. The exact values of  $Re_c$  and  $Re_c^*$  are dependent on  $\alpha$  and will be elucidated later but for convenience are specified in advance in Table I.

## B. Flow field measurements

A micro-particle image velocimetry ( $\mu$ -PIV) system (TSI, Inc., MN) is used in order to perform quantitative measurements of the flow field.<sup>53,54</sup>

For flow visualization, the test fluids are seeded with fluorescent particles (PS-FluoRed, MicroParticles GmbH, Germany) of diameter  $d_p = 5.0 \mu\text{m}$  with excitation and emission wavelengths of 530 nm and 607 nm, respectively. The microfluidic devices are mounted on the stage of an inverted microscope (Nikon Eclipse Ti), and a Nikon Plan Fluor,  $4\times$ ,  $NA = 0.13$  numerical aperture lens is used to bring the central  $x = 0$  plane into focus [Fig. 1(a) (Multimedia view)]. With this combination of particle size and objective lens, the measurement depth over which particles contribute to the determination of the velocity field is  $\delta x_m \approx 210 \mu\text{m}$  ( $\delta x_m < 0.33w$ ).<sup>53</sup> Using a dual-pulsed laser synchronized with a high-speed camera operated in frame-straddling mode, particle images are captured in pairs with a known time separation. By cross-correlating the images in each pair, velocity vectors  $v_y$  and  $v_z$  are obtained in the  $y$  and  $z$  directions, respectively. Further specifications about the  $\mu$ -PIV system and the measurement and processing methods can be found in a previous publication.<sup>14</sup>

## C. Experimental protocol

Quasistatic experiments are conducted over a range of  $Re_c < Re < Re_c^*$  by programming the syringe pumps to perform ramps up and down in  $Re$  with small step increases or decreases of  $0.2 \lesssim \Delta Re \lesssim 2$  (depending on the specific microfluidic device under study). Five seconds of steady flow is imposed at each increment in  $Re$ . Note that this is significantly longer than the diffusion time scale of water calculated for the device with the largest length scale ( $\alpha = 0.45$ ,  $w = 1490 \mu\text{m}$ ), which is given by  $t_d = (w/2)^2/\nu \approx 0.56$  s.

Image pairs are captured at a rate of 5 Hz using the  $\mu$ -PIV system. For each step in  $Re$ , 25 velocity vector fields are thus produced. The velocity fields from each step are averaged (avoiding transients) using the software Tecplot Focus (Tecplot, Inc., WA), and the averaged flow field is further processed to obtain the streamwise vorticity  $\omega_x = (\partial v_z/\partial y) - (\partial v_y/\partial z)$  and streamline projections on the  $x = 0$  plane.

Based on the values of  $Re_c$  and  $Re_c^*$  found in the quasistatic experiments (given already in Table I), time dependent measurements are conducted. The transition from symmetric to asymmetric flow is studied by imposing a single step in  $Re$  from an initial value  $Re_i < Re_c^*$  to a final value  $Re_f > Re_c^*$ . Similarly, the opposite experiments are conducted with a single step in  $Re$ , from  $Re_i > Re_c$  to a final value  $Re_f < Re_c$ . For each value of  $\alpha$ , several measurements are performed for various values of  $Re_f$ , while  $Re_i$  is held constant. Data acquisition starts before flow is imposed. The Reynolds number is increased from 0 to  $Re_i$  and held steady for 5 s. Subsequently,  $Re$  is increased from  $Re_i$  to  $Re_f$  and again the flow is kept steady for 5 s. By this protocol, we can easily determine the moment during acquisition where the second step begins, which defines the time  $t = 0$ . In these experiments, image pairs are captured at 100 Hz and are processed individually to

obtain 100 velocity fields per second. This is found to be more than sufficient to capture the detailed dynamics of the flow transition.

#### D. Landau model

As in a number of previous studies,<sup>13,14,55</sup> the Landau model of equilibrium phase transitions is used here to describe symmetry breaking flow transition.

We use a dimensionless order parameter  $\psi$  to represent the degree of symmetry in the flow,

$$\psi = \frac{\int_{-\frac{d}{2}}^{\frac{d}{2}} \int_{-\frac{d}{2}}^{\frac{d}{2}} \omega_x dz dy}{\int_{-\frac{d}{2}}^{\frac{d}{2}} \int_{-\frac{d}{2}}^{\frac{d}{2}} |\omega_x| dz dy}. \quad (2)$$

For symmetric flow ( $Re < Re_c^*$ ), the two pairs of co-rotating diagonally opposed Dean vortices are of equal and opposite magnitude; hence, the numerator in Eq. (2) vanishes and  $\psi = 0$ . For  $Re > Re_c$ , one of the pairs of co-rotating Dean vortices intensifies at the expense of the other [as shown in Fig. 1(d) (Multimedia view)] and  $\psi$  attains a non-zero value.

A sextic Landau-type polynomial potential is used to describe the symmetry-breaking bifurcation<sup>13,14,56</sup>

$$F = -h\psi - \frac{1}{2}\varepsilon\psi^2 + \frac{1}{4}g\psi^4 + \frac{1}{6}k\psi^6, \quad (3)$$

where  $\varepsilon = (Re - Re_c)/Re_c$  is a normalized control parameter.

The value of  $\psi(\varepsilon)$  corresponds to the extrema of  $F$ , where  $\partial F/\partial\psi = 0$  and therefore  $\varepsilon$  can be written in the following form:<sup>13</sup>

$$\varepsilon = k\psi^4 + g\psi^2 - h\psi^{-1}. \quad (4)$$

The ratio between the coefficients  $g$  and  $k$  determines the shape and order of the transition. When  $g > 0$ , the forward bifurcation at  $\varepsilon = 0$  is analogous to a supercritical phase transition. For  $g < 0$ , the bifurcation turns backwards, corresponding to a subcritical phase transition with hysteresis. In the special case of  $g = 0$ , the transition lies between super and subcritical, and the bifurcation at  $\varepsilon = 0$  is termed “tricritical.” The asymmetric term with the coefficient  $h$  accounts for system imperfections that lead to the selection of a favored co-rotating vortex pair to intensify at the expense of the other pair. Note that  $\psi$  can be either positive or negative, depending on which pair of Dean vortices dominates and merges for  $\varepsilon > 0$ . For clarity of presentation of our results, we define an additional quantity  $\psi' = \psi \operatorname{sgn}(\psi|_{\varepsilon>0})$ , for which the dominant branch of instability appears positive regardless of the direction of vortex rotation.

### III. RESULTS

#### A. Quasistatic control of Re

In this section, we present the results of quasistatically controlled ramps of increasing and decreasing  $Re$  carried out in the four cross-slot devices with different values of  $\alpha$ . We begin by characterizing in detail the flow bifurcation in each

device in terms of the Landau model (from which we produce a phase diagram for the transitions). We then proceed to analyse the associated approach and separation of the dominant Dean vortex pair.

#### 1. Flow bifurcation and the Landau potential

The quantity  $\psi'$  (which captures the degree of asymmetry in the flow) is plotted as a function of the normalized control parameter  $\varepsilon$  for all four values of  $\alpha$  in Fig. 2. Increasing ramps in  $Re$  are represented by solid symbols and decreasing ramps by open symbols. In all cases, the data are well described by Eq. (4) (solid lines), from which we obtain the parameters  $g$ ,  $k$ ,  $h$ , and  $Re_c$ . For subcritical transitions ( $g < 0$ ), we also obtain  $Re_c^* = Re_c(1 - g^2/4k)$  (for  $g \geq 0$ ,  $Re_c^* = Re_c$ ). The values obtained for  $Re_c$  and  $Re_c^*$  are summarized in Table I. Additional details about the parameters extracted from the Landau model can be found in the [supplementary material](#).

Consistent with expectations,<sup>13</sup> our data reveal that a supercritical transition occurs at the lowest aspect ratio,  $\alpha = 0.45$  [Fig. 2(a)]. An essentially tricritical transition is observed for  $\alpha = 0.57$  [Fig. 2(b)], for which the transition appears slightly backwards, but  $Re_c^* = Re_c$  within experimental error. Clearly subcritical transitions occur at  $\alpha = 1.1$  and  $\alpha = 2.4$ , with small and larger hysteresis loops, respectively [Figs. 2(c) and 2(d)].

From Table I, we can see that  $Re_c$  increases as  $\alpha$  is decreased. The confinement of the flow field by the solid channel walls at  $z = \pm d/2$  increasingly stabilizes the flow as

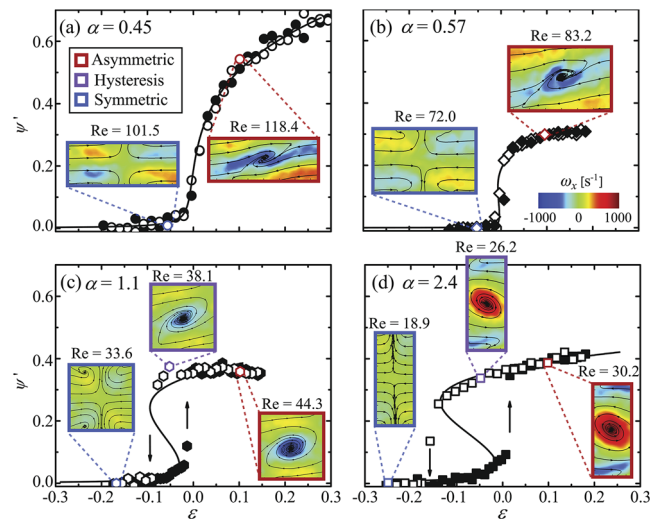


**FIG. 2.** The order parameter  $\psi'$  (multiplied by its own sign for  $\varepsilon > 0$ ) as a function of the control parameter  $\varepsilon$  for quasistatic measurements in cross-slot channels with different aspect ratios,  $\alpha$ . (a) Supercritical transition for  $\alpha = 0.45$ , (b) near tricritical transition for  $\alpha = 0.57$ , (c) subcritical transition with a small hysteresis loop for  $\alpha = 1.1$ , and (d) a larger hysteresis loop for  $\alpha = 2.4$ . Closed and open symbols represent data obtained by controlled increases and decreases in  $Re$ , respectively. Curves are fitted with the Landau model [Eq. (4)]. Arrows indicate the jump between stable and unstable branches where hysteresis is detected. Insets are  $\mu$ -PIV images of the vorticity at the center plane ( $x = 0$ ) at the values of  $Re$  indicated above each image.

$\alpha$  is decreased, and therefore a higher  $Re_c$  is needed for the symmetric flow state to become unstable.

The insets of Fig. 2 show contour plots of the vorticity over the  $x = 0$  plane with streamline projections superimposed. These plots demonstrate the flow field for decreasing  $Re$  ramps. The flow fields enclosed by a red frame show a single spiral vortex structure for  $\varepsilon = 0.1$ . The flow field enclosed by a blue frame corresponds to symmetric flow at  $Re < Re_c^*$ . For  $\alpha = 0.45$  and  $\alpha = 0.57$ , the symmetric flow state is regained for  $\varepsilon \leq 0$  [see Figs. 2(a) and 2(b)]. For the channels with higher  $\alpha = 1.1$  and  $\alpha = 2.4$ , the regaining of symmetry happens at lower values of  $\varepsilon \leq -0.1$  and  $\varepsilon \leq -0.18$  (respectively), due to the hysteresis [Figs. 2(c) and 2(d)]. For these cases, we show an additional inset flow field (enclosed in a mauve frame) for conditions within the hysteresis loop, where  $\varepsilon = -0.05$ .

Varying  $\alpha$  and  $\varepsilon$  results in a change of the shape of the Landau potential and the free energy of the system. The Landau potentials [ $F(\psi)$ , Eq. (3)] can be calculated from the parameters used to fit Eq. (4) to the experimental bifurcation diagrams in Fig. 2. Examples of  $F(\psi)$  for various  $(\alpha, \varepsilon)$  are shown as insets in the phase diagram presented in Fig. 3. The vertical red line in Fig. 3 marks the aspect ratio  $\alpha = 0.55$  for which a tricritical point is formed at  $\varepsilon = 0$ . To the left hand side of the red line, the transition will be supercritical, and to the right hand side, the transition will be subcritical. The black horizontal line marks the line of critical points, where  $\varepsilon = 0$ . The dashed-dotted black line marks the hysteretic curve, where  $\varepsilon = g^2/4k$ . Below the dashed-dotted line,  $F$  has a single minimum at  $\psi = 0$ , indicating that symmetric flow is always the only stable state. Above the solid black line, for  $\varepsilon > 0$ ,  $F$  has a maximum at  $\psi = 0$  (symmetric flow becomes unstable), and acquires two new minima, the new stable points, where the flow is asymmetric. The left-hand-side minimum corresponds

to a negative solution ( $\psi < 0$ , clockwise rotation), while the right-hand-side minimum corresponds to a positive solution ( $\psi > 0$ , counter-clockwise rotation). Since the bifurcations in these experiments are not perfect, and we get a non-zero  $h$  term in Eq. (3), one minimum will be deeper than the other, and to this deeper well, the instability will evolve corresponding to the direction of the vortex rotation. Between the black solid line and the black dashed-dotted line is the hysteretic region in which  $F$  has three minima and the symmetric state can be either stable or unstable, depending on the history of the system.

As  $\varepsilon$  is increased up to the onset of the asymmetry, and  $\psi$  becomes non-zero, a dominant pair of co-rotating Dean vortices begin to approach each other in the process of merging. In Sec. III A 2, we describe for the first time, a controlled merging process captured during quasistatic experiments. We will also present the data from the opposite experiments, in which a single vortex splits into two co-rotating vortices that migrate away from each other as  $\varepsilon$  is decreased in a quasistatic fashion.

### 2. Quasistatic vortex merging and splitting

In the process of vortex merging, two co-rotating vortices grow in size and share their outer vorticity bands as they approach each other. This process and its mechanism have been described in detail in the literature for unconfined macroscale vortices.<sup>28-36</sup> The first stage of merging is characterized by diffusive growth of the vortex cores and a slow approach of the cores towards each other. Typically, once the ratio between core size  $a$  and core separation distance  $b$  has reduced to a value  $0.24 \leq a/b \leq 0.32$ , a convective merging stage will begin. In the fast convective stage, the vortices deform, share filaments, and rapidly move toward each other. The final third stage is the merged diffusive stage in which the two vortices are merged into a single structure.<sup>31,57,58</sup> Some studies have reported a fourth stage in the merging process, which is referred to as a second diffusive stage (a slowdown in the merging process), that follows the convective stage, prior to the ultimate merging.<sup>29-31</sup>

In all of the previous reports, the experiments were time dependent, where only the initial  $Re$  was controlled.<sup>28,30,57-60</sup> Here, with quasistatic experiments, we are able to precisely control  $Re$  in very small increments, which allows us to arrest the merging process at any stage while maintaining a constant background flow. To the best of our knowledge, such a controlled experimental system for the study of vortex merging has not been reported before.

Additionally, in previous studies, the vortices were not confined and therefore were able to move freely and rotate around each other in the process of merging. This rotation is eliminated from our experimental system in which each Dean vortex is confined to a quadrant of the channel cross section, due to the boundaries dictated by the neighboring counter vortices and the walls of the channel. Our experimental system thus allows us to completely avoid a rotating reference frame and consequently maintain a uniform and simplified data analysis.<sup>38,48</sup>

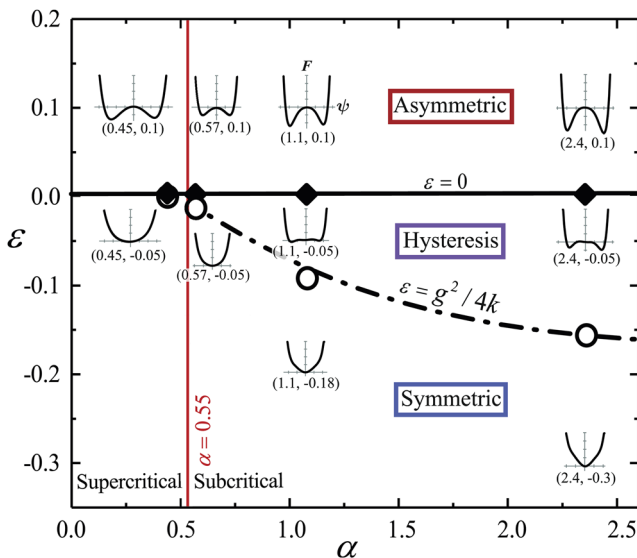


FIG. 3. Phase diagram for transitions in  $(\alpha, \varepsilon)$  parameter space.

The process of merging is commonly studied by following the distance between the cores of the merging vortices,  $b$ , normalized by the maximal distance between the cores  $b_0$ .<sup>39</sup> In order to identify the location of the cores, we first need to define the planar domain in which the vortex is confined and find the circulation of the Dean vortex ( $\Gamma_{Dean}$ ) within the domain. In our experiments, it is reasonable to assume that the planar domain for each Dean vortex is its respective quadrant of the cross section of the channel. The circulation in each quadrant,  $\Gamma_{Dean}$  is given by

$$\Gamma_{Dean} = \int_0^{\pm \frac{w}{2}} \int_0^{\pm \frac{d}{2}} \omega_x dz dy. \quad (5)$$

Of course, in the present experimental system, an equivalent analysis can also be performed for vortex splitting, i.e.,  $b$  can be evaluated as  $Re$  is progressively reduced as well as increased for  $Re < Re_c$ .

In Fig. 4, the nondimensionalized average circulation of the two merging Dean vortices  $\Gamma_{Dean}/Uw$  is plotted as a function of  $\varepsilon$  for  $\varepsilon < 0$ . From this figure, we can see that the maximal dimensionless circulation of a Dean vortex is measured just before the onset of the asymmetric flow. We note that near  $\varepsilon = 0$  the dimensional circulation is higher in channels with lower  $\alpha$  (as illustrated by the inset images). However, in dimensionless form  $\Gamma_{Dean}/Uw$  is higher for  $\alpha = 1.1$  and  $2.4$  than it is for  $\alpha = 0.57$  and  $0.45$ , even though the Reynolds number has now effectively been scaled out and a data collapse might be expected.

The insets of Fig. 4 show the vorticity of the flow field at  $x = 0$  for  $\varepsilon = -0.02$ , just before the onset of the asymmetric

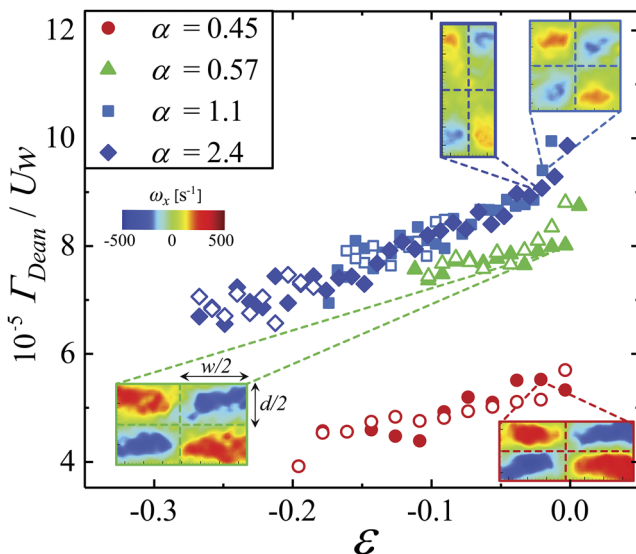


**FIG. 4.** The nondimensional circulation  $\Gamma_{Dean}/Uw$  of a quadrant from the cross section at  $x = 0$  is plotted as a function of  $\varepsilon$ . Closed and open symbols correspond to increasing and decreasing increments in  $Re$ . Insets are  $\mu$ -PIV images of the vorticity at  $x = 0$  for  $\varepsilon = -0.02$ , and the dashed lines divide the flow field into the defined quadrants.

flow. The vorticity patches shown in the insets of Fig. 4 give an indication of the space within the quadrant occupied by a Dean vortex. For  $\alpha = 0.45$  and  $0.57$ , the vorticity patches occupy nearly the entire quadrant. The size of the Dean vortex is set by the channel half-width  $w/2$ , so for  $\alpha < 1$  the Dean vortices are compressed by the shallow depth and are constricted between the wall and the counter rotating vortices. By contrast, for higher  $\alpha > 1$ , the vorticity patches are localized near the walls at  $z = \pm d/2$ , occupy a space that is smaller than the quadrant, and are therefore less spatially confined.

The center position of the merging Dean vortices  $X^c$  is calculated from the velocity field as follows:<sup>39</sup>

$$X^c = \frac{1}{\Gamma_{Dean}} \int_0^{\pm \frac{w}{2}} \int_0^{\pm \frac{d}{2}} X \omega_x dz dy, \quad (6)$$

where  $X$  is the coordinate within the quadrant containing the vorticity  $\omega_x$ . After finding the center position of each Dean vortex for each imposed  $Re$ , the distance between the two merging vortices ( $b$ ) is computed by subtraction.

The parameter  $b/b_0$  is plotted as a function of  $\varepsilon$  in Fig. 5(a), where closed and open symbols refer to vortex merging (increasing  $\varepsilon$ ) and vortex splitting (decreasing  $\varepsilon$ ), respectively.

In low aspect ratio channels ( $\alpha < 1$ ), we observe that the approach of the dominant Dean vortex pair with increasing  $\varepsilon$  is very gradual and actually continues beyond the onset of symmetry breaking. Merging into a single central vortex occurs after displacement of the Dean vortices through a relatively short distance ( $\approx 0.1b_0$ ). Since the Dean vortices are relatively close to each other even in the symmetric state (see insets of Fig. 4), merging occurs for a relatively small displacement of the cores.

For the deep channels with  $\alpha > 1$ , the two merging Dean vortices show an initially gradual approach as  $\varepsilon$  is increased but then rapidly merge into a single structure at  $\varepsilon = 0$ . In these cases, the Dean vortices are more widely separated in the symmetric flow state (see insets of Fig. 4), so must displace a considerable fraction of their maximal separation  $b_0$  before merging occurs.

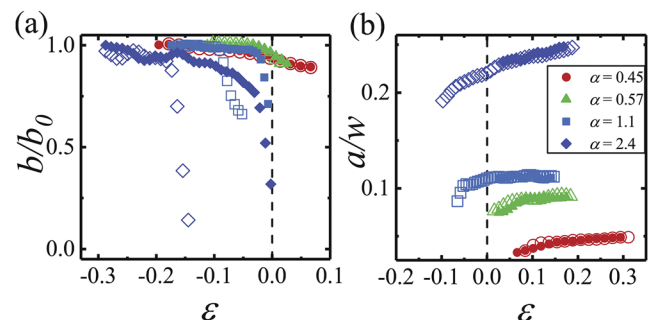


**FIG. 5.** (a) Normalized distance between Dean vortex pairs prior to merging,  $b/b_0$  as a function of  $\varepsilon$ . (b) Normalized characteristic radius  $a/w$  of the single merged vortical structure as a function of  $\varepsilon$ . Closed/open symbols represent increasing/decreasing  $Re$  steps.

Apart from the vortex merging process, our experimental system allows the controlled study of vortex splitting. Vortex splitting was theoretically predicted decades ago and was supported with computational evidence.<sup>61–63</sup> Experimental observations of vortex splitting were first reported by Freymuth *et al.*<sup>41,42</sup> Their experiments validated the previous theoretical predictions, by the observation of vortex splitting behind an airfoil where regions of vorticity of opposite signs were formed (a flow field somewhat resembling that in our own experiments, see Fig. 2). Later on, numerical simulations revealed that the process of merging and splitting of Dean vortex pairs, in curved and rotating channel flows, could be attributed to spanwise perturbations known as the Eckhaus instability.<sup>43</sup> Additional reports suggest that merging and splitting events in arrays of counter-rotating Dean vortices are associated with the spacing between vortex pairs and are affected by centrifugal instabilities.<sup>44</sup> Yet in all of the mentioned studies the control over the experimental conditions was limited. Additionally, the previous studies involved stacks of multiple vortices that exhibit complex interactions. By contrast, in our experimental setup, a single vortex is isolated at a fixed location and forced to split in a controlled fashion by a simple manipulation of the Reynolds number.

In our experiments, we are able to measure the separation between vortices as we reduce  $Re$  in a finely controlled manner, as demonstrated by the open symbols in Fig. 5(a). For the low  $\alpha$  channels, the merging and splitting processes are clearly reversible as the curves follow the same path. However, for  $\alpha = 1.1$  and  $2.4$ , the vortex splitting occurs for lower values of  $\varepsilon$  than vortex merging. This is due to the hysteresis in the flow that permits the existence of a central vortex for  $-g^2/4k < \varepsilon < 0$ .

Once the dominant Dean vortex pair has merged into a single central vortex, we can continue our analysis by tracking the size of the vortex core as a function of the imposed  $\varepsilon$ . The characteristic radius of the central vortex core is evaluated from the second order moment of vorticity<sup>39</sup>

$$a^2 = \frac{1}{\Gamma} \int_{-\frac{w}{2}}^{\frac{w}{2}} \int_{-\frac{d}{2}}^{\frac{d}{2}} |X - X^c|^2 \omega_x dz dy. \quad (7)$$

The vortex core radius is normalized by the characteristic length scale  $w$  and is plotted as a function of  $\varepsilon$  in Fig. 5(b). For increasing  $Re$  ramps, the plots show how the radius of the central vortex core increases with increasing  $\varepsilon$ , starting from the value at which the merging process is completed and the central vortex is formed. For  $\alpha = 0.45$  and  $0.57$ , the growth and reduction of the central vortex radius as  $Re$  is increased and decreased clearly follow the same curve. However for  $\alpha = 1.1$  and  $2.4$  the curve for reducing  $Re$  is prolonged to negative values of  $\varepsilon$  and smaller values of  $a/w$  due to the hysteresis in the flow. As  $\alpha$  is increased, the central vortex occupies a greater portion of the channel width  $w$ . However, the size of the central vortex is not limited simply by  $w$  since the vortex can actually impinge into the channel inlets [as reported previously<sup>13</sup> and demonstrated by the inset in

Fig. 2(d) where  $Re = 30.2$ ]. This implies that the central vortex size is mostly limited by  $d$ , the depth of the channel. Therefore, higher values of  $\alpha$  enable relatively larger, more intense vortices to be formed, while low  $\alpha$  suppresses vortex growth and intensification.

## B. Dynamic experiments

In this section, we will describe the dynamic flow experiments in which we impose a large step increase or decrease in  $Re$  across the critical value and observe the time evolution of the flow as it approaches the steady state. We begin by presenting the time dependence of the symmetry breaking flow instability before describing the dynamics of the associated vortex merging and splitting processes.

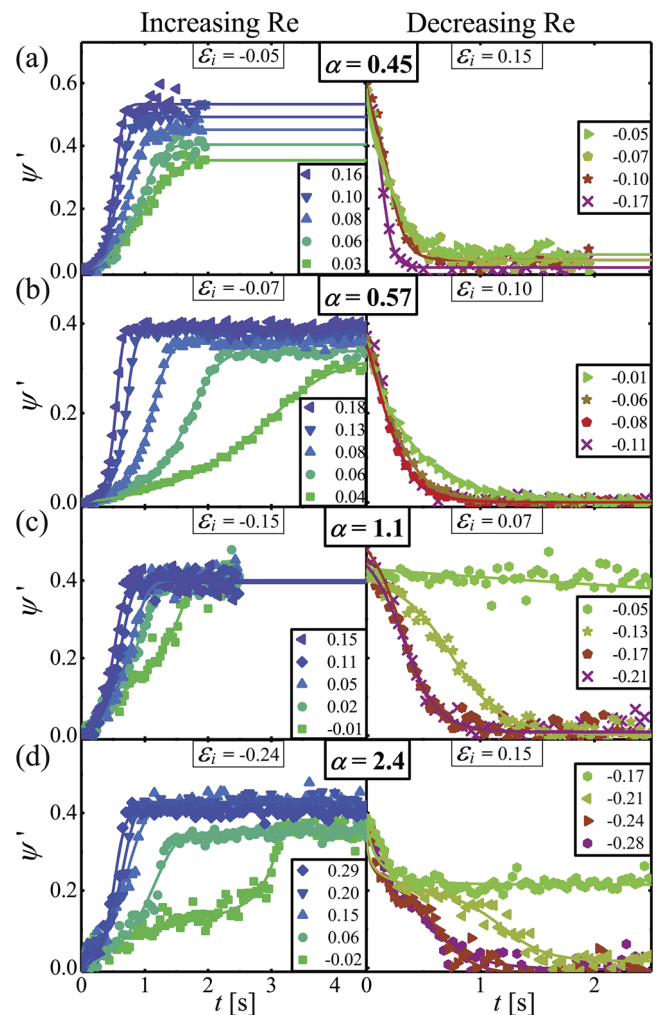


**FIG. 6.** Time dependence of  $\psi'$  for all four aspect ratios: (a)  $\alpha = 0.45$ , (b)  $\alpha = 0.57$ , (c)  $\alpha = 1.1$ , and (d)  $\alpha = 2.4$ . Experiments are done for various values of  $\varepsilon_i$ , indicated in the legends. The data are fitted with the dynamic form of the Landau model [Eq. (8)]. (Left) Increasing  $Re$  steps and (right) decreasing  $Re$  steps.

### 1. Dynamics of the flow transition

Time dependent experiments are conducted by imposing a single step increase or decrease in  $Re$  from an initial value  $Re_i$  to a final value  $Re_f$  across the transition, as described in Sec. II C. This results in an instantaneous change in the free energy of the system  $F$ . We follow  $\psi$  as it subsequently evolves in time towards equilibrium in one of the new potential wells (see insets in Fig. 3).

For time dependent experiments, the initial and final imposed control parameters are defined as  $\varepsilon_i = (Re_i - Re_c)/Re_c$  and  $\varepsilon_f = (Re_f - Re_c)/Re_c$ , respectively.

For increasing  $Re$  steps, we begin with an initial  $Re_i < Re_c^*$  and end with a final  $Re_f > Re_c^*$ . The left-side column of Fig. 6 shows  $\psi'$  plotted as a function of time ( $t$ ) for increasing  $Re$  steps, from  $\varepsilon_i$  (indicated in the figure) to various values of  $\varepsilon_f$  which are specified in the legend.

For experiments involving decreasing  $Re$  steps, we begin from an initial  $Re_i > Re_c$  (i.e.,  $\varepsilon_i > 0$ ) and reduce to a final  $Re_f < Re_c$  (i.e.,  $\varepsilon_f < 0$ , including values within the hysteresis regions). The curves showing  $\psi'(t)$  for decreasing  $\varepsilon$  experiments are plotted in the right-side column of Fig. 6, where again  $\varepsilon_i$  is indicated in the figure and the various values of  $\varepsilon_f$  imposed at each aspect ratio are indicated in the legends.

The solid lines in Fig. 6 are fits to the data curves using a dynamic form of the Landau model<sup>56</sup>

$$\tau \frac{d\psi}{dt} = -\frac{dF}{d\psi} = \varepsilon\psi - g\psi^3 - k\psi^5 + h, \quad (8)$$

where  $\tau$  is a characteristic time.

In order to reduce the number of free parameters in this fit,  $k$  was set to be equal to 1. The parameters  $g$ ,  $h$ ,  $\varepsilon$ , and  $\tau$  were left free, and their specific values are discussed in detail in the supplementary material. As is evident from Fig. 6, Eq. (8) provides an excellent description of the relaxation dynamics observed in our experiments at all  $\alpha$  and  $\varepsilon_f$ .

For increasing steps in  $\varepsilon$  (Fig. 6, left), the results are in general accordance with the quasistatic flow curves shown in Fig. 2 and the steady state value of  $\psi'$  grows as the imposed  $\varepsilon_f$  is increased. For the subcritical transitions, we note some interesting cases, e.g., for  $\alpha = 2.4$  at  $\varepsilon_f = -0.02$ , where  $\psi'$  appears to settle at an intermediate metastable value for  $1 \lesssim t \lesssim 2.5$  s before eventually increasing to the final steady state value. The intermediate and final values of  $\psi'$  are approximately consistent with the values found on the lower and upper branches within the hysteresis loop shown in Fig. 2(d) at the same  $\varepsilon = \varepsilon_f = -0.02$ . Despite the resulting complex time evolution of  $\psi$ , Eq. (8) captures the dynamics in a very precise manner.

From the plots in Fig. 6 (left), it is apparent that the transition becomes prolonged as  $\varepsilon_f$  is decreased. This can be explained by the change in shape of the Landau potential. For small values of  $\varepsilon_f$ , the new potential wells that form are shallow and therefore  $F$  at  $\psi = 0$  is nearly flat, which causes  $\psi$  to evolve slowly. A larger  $\varepsilon_f$  results in deeper potential wells with steeper slopes near  $\psi = 0$  which cause the transition to occur faster. This trend is seen for all values of  $\alpha$  that are studied here; however, the slowdown in the dynamics of the transition is most prominent near the tricritical point [i.e., for  $\alpha = 0.57$  as  $\varepsilon_f \rightarrow 0$ , Fig. 6(b)]. Similar behaviors have also been reported for flow transitions near critical points in the Taylor–Couette geometry.<sup>64,65</sup>

The right-hand side of Fig. 6 shows the evolution of  $\psi'$  as  $\varepsilon$  is decreased from  $\varepsilon_i > 0$  to  $\varepsilon_f < 0$ . From these plots, it is seen that for lower aspect ratios [Figs. 6(a) and 6(b)] the transition back to symmetry (i.e.,  $\psi = 0$ ) occurs faster than the symmetry breaking even as  $\varepsilon_f \rightarrow 0$ . This can again be explained simply by considering the change in shape of the Landau potential, which changes directly from having two minima to having a single minimum as  $\varepsilon_f$  is decreased below the critical value (see insets in Fig. 3). For the subcritical transitions at higher aspect ratios [Figs. 6(c) and 6(d)], where hysteresis

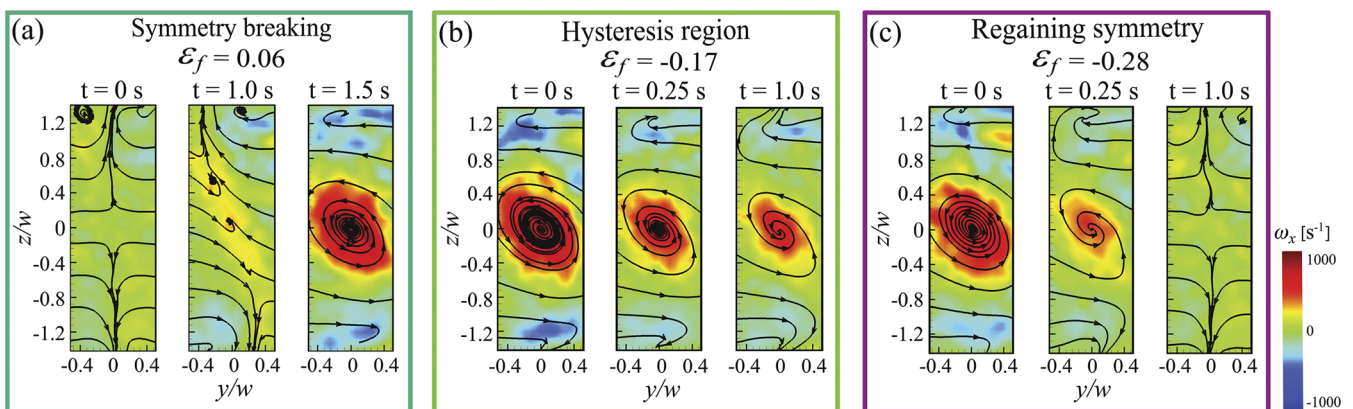


**FIG. 7.** Evolution of vorticity fields observed in the center plane ( $x = 0$ ) of a cross-slot device with  $\alpha = 2.4$ . (a) Symmetry breaking and formation of a central vortex are captured for an increase from  $\varepsilon_i = -0.24$  to  $\varepsilon_f = 0.06$ . (b) Decay of a central vortex for a reduction from  $\varepsilon_i = 0.15$  to  $\varepsilon_f = -0.17$  (within the hysteresis loop). (c) Regaining of symmetric flow for a reduction from  $\varepsilon_i = 0.15$  to  $\varepsilon_f = -0.28$ . The colored frames surrounding the sets of images correspond to the data sets shown in Fig. 6(d). Multimedia views: <https://doi.org/10.1063/1.5087732.2>; <https://doi.org/10.1063/1.5087732.3>; <https://doi.org/10.1063/1.5087732.4>

emerges, the process of regaining symmetry is more complicated, as seen by the convoluted curve shapes. For values of  $-g^2/4k < \varepsilon_f < 0$  that lie within the hysteresis loop, the Landau potential develops three minima (see Fig. 3) and it is possible to remain at a high value of  $\psi'$  in a stable or metastable state.

Figure 7 (Multimedia view) shows the flow vorticity fields measured in dynamic experiments for three different cases of a subcritical transition ( $\alpha = 2.4$ ). For an increase in  $\varepsilon$  from  $\varepsilon_i = -0.24$  to  $\varepsilon_f = 0.06$ , Fig. 7(a) (Multimedia view) shows how the flow field breaks symmetry at  $t > 0$  and evolves to a stable asymmetric field with a fully developed central vortex. This set of figures corresponds to the plot shown in Fig. 6(d), where  $\varepsilon_f = 0.06$  (turquoise circles). The evolution of the flow for a reduction of  $\varepsilon$  from  $\varepsilon_i = 0.15$  into the hysteresis region is shown by the images in Fig. 7(b) (Multimedia view), where  $\varepsilon_f = -0.17$ . Here, the flow field evolves from stable central vortex at  $t = 0$  s to a smaller central vortex at  $t = 0.25$  s and finally to an even smaller vortex at  $t = 1$  s that subsequently remains stable and steady in time. This set of figures corresponds to the plot shown in Fig. 6(d), where  $\varepsilon_f = -0.17$  (bright green symbols). Regaining of symmetric flow from an initially asymmetric state at  $\varepsilon_i = 0.15$  is illustrated by Fig. 7(c) (Multimedia view), for  $\varepsilon_f = -0.28$  [corresponding to the dark red symbols in Fig. 6(d)]. Here we can see how the flow field is transformed from a fully developed central vortex back to a symmetric state within  $\approx 1$  s.

In Sec. III B 2, we will focus on analysing the dynamics of confined merging vortices and the opposite process in which a single vortex splits into two vortices.

## 2. Dynamics of vortex merging and splitting

The normalized separation distance between vortices  $b/b_0$  is plotted as a function of dimensional time in Fig. 8. The left hand side of Fig. 8 shows the data for increasing Re experiments during the process of merging. The right hand side of Fig. 8 shows the opposite experiments where a step decrease in Re causes the single central vortex to split into two Dean vortices that migrate away from each other towards the channel walls.

We notice that for  $\alpha = 0.45$  and  $0.57$  the range of movement of the Dean vortices prior to merging is  $\approx 0.1b_0$  [Figs. 8(a) and 8(b)], similarly to the finding in the quasistatic experiments shown in Sec. III A. For  $\alpha = 1.1$ , the range of movement is  $\approx 0.5b_0$  [Fig. 8(c)], while for the highest aspect ratio  $\alpha = 2.4$ , we observe that the Dean vortices pass through an even larger relative distance  $\approx 0.7b_0$  before merging [Fig. 8(d)]. The merging process that is seen for  $\alpha = 1.1$  and  $\alpha = 2.4$  has a qualitative similarity to previous studies in which the vortices are not confined.<sup>30,31,57,58,66,67</sup>

Since the experimental system enables control of the initial and final Re, we are able to capture unique cases in which the vortices are in the process of merging but never fully merge, due to the balance achieved between inertial and viscous forces at the final  $Re_f$ . Examples for this equilibrium state within the vortex merging process can be seen for two experiments with the channel  $\alpha = 0.45$  for

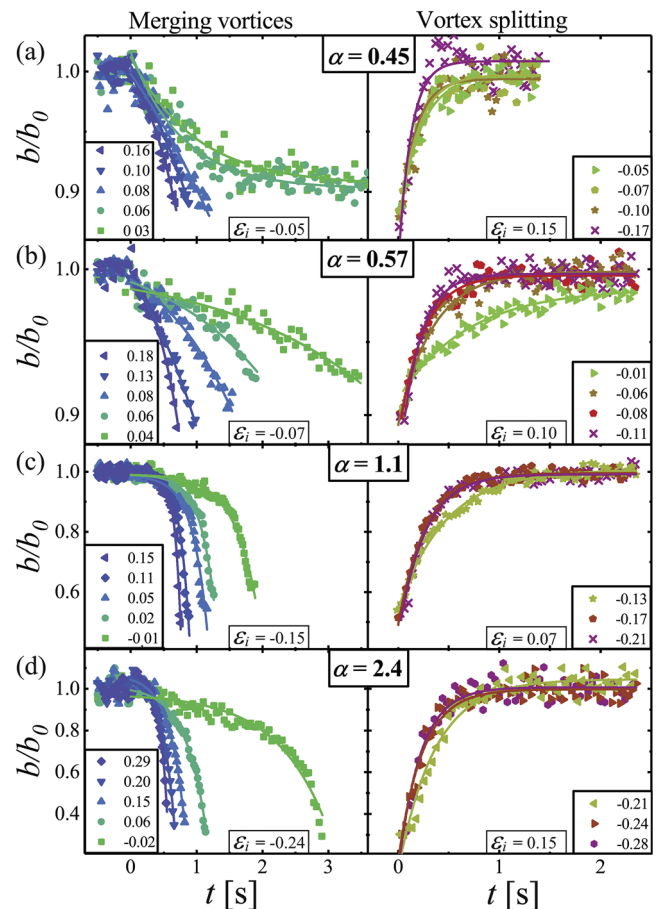


**FIG. 8.** Normalized distance between the center position of merging and separating Dean vortices ( $b/b_0$ ) as a function of time for four aspect ratios; (a)  $\alpha = 0.45$ , (b)  $\alpha = 0.57$ , (c)  $\alpha = 1.1$ , and (d)  $\alpha = 2.4$ . Experiments are performed for step increases (left) and decreases (right) in  $\varepsilon_f$ , which is indicated in the legend. Solid lines correspond to exponential curve fitting.

which  $\varepsilon_f = 0.03$  and  $\varepsilon_f = 0.06$  [as shown in the left side of Fig. 8(a)]. By fixing  $Re_f$  in the dynamic experiments, we are also able to arrest the process at any given stage while remaining under constant flow. This can potentially enable a very detailed study of the flow field during merging and splitting of vortices.

In order to get further insight into the effects of confinement on the dynamics of the merging and splitting processes we performed curve fitting to the plots in Fig. 8 at different aspect ratios. All of our experimental data sets (for vortex merging and the splitting) are well-described by a simple exponential of the form  $b/b_0 = 1 + Ae^{R_0 t}$ , where  $A$  is a constant and  $R_0$  is the rate of the exponential growth. Note that vortex merging has been described as an exponential process in various previous studies.<sup>27,36,68–71</sup> The parameter  $R_0$  is extracted from the exponential data fit and is plotted as a function of  $\varepsilon_f$  in Fig. 9.

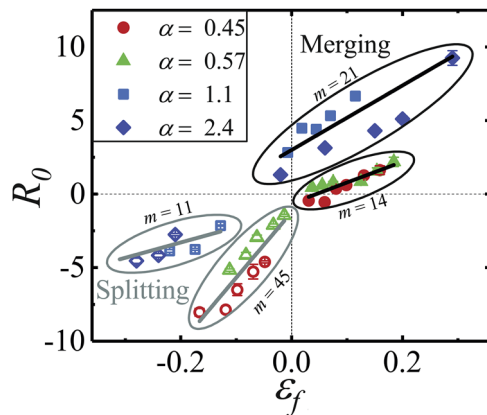


**FIG. 9.**  $R_0$  as a function of  $\varepsilon_f$ .  $R_0$  is extracted from the exponential fits to the data in Fig. 8(a). The solid lines are linear fits to the data, where  $m$  is the slope. Merging data are located in the upper right quadrant; splitting data are located in the lower left quadrant.

From our results, it is seen that the rates of both the merging and the splitting processes are linearly dependent on the imposed  $\varepsilon_f$ , with an apparent change in slope at the critical point.

Considering first the merging process, at all aspect ratios we observe faster merging for higher  $\varepsilon_f$ . This is in agreement with previous experiments which measured the time taken for vortices to merge for different initial imposed  $Re$ .<sup>29</sup>

For a given  $\varepsilon_f$ , merging rates are faster in high  $\alpha$  devices compared to the low  $\alpha$  channels.

Now, considering the splitting process, we observe the opposite trend, i.e., faster splitting in low  $\alpha$  channels than in high  $\alpha$  channels (for a given  $\varepsilon_f$ ).

Considering only the low  $\alpha$  channels, it is apparent that, equidistant from the critical point, the merging is significantly slower than the splitting of vortices. The opposite is true for high  $\alpha$  channels, where merging proceeds at a faster rate than splitting.

The contrasting dynamics can be attributed to the higher value of  $\Gamma_{Dean}/Uw$  (see Fig. 4) that leads to stronger attraction between Dean vortices in high  $\alpha$  channels. Hence the vortices in high  $\alpha$  channels are relatively quick to merge but relatively slow to separate in comparison with lower  $\alpha$  channels. This disparity provides a basis for understanding the hysteresis in the flow transition observed in the higher aspect ratio channels.

Confining vortices by reducing the channel aspect ratio forces them to be in an “unnatural” constricted environment. At higher aspect ratios, the vortices are less confined, show a more natural circular shape and gain further spatial freedom. Consequently, we can expect that in an unconfined system (for instance in aerodynamics or geophysical flows), the splitting dynamics will be slower than that of merging.

In Sec. III B 3, we will discuss the relation between the onset of the flow instability and regaining of symmetry with the merging and splitting of vortices.

### 3. Relation between flow instability and vortex dynamics

Here, we present the relation between the order parameter  $\psi$ , which describes the degree of flow asymmetry, and the distance between the merging and separating Dean vortices  $b$ .

For each  $\alpha$ , the plots of  $\psi'$  as a function of  $1 - b/b_0$  are presented in Fig. 10 for a wide variety of  $\varepsilon_f$ . In general, there is a good collapse of the data at each aspect ratio, clearly showing the inter-relation between the two quantities and suggesting that  $\psi'$  depends only on the distance between Dean vortices, independently of the history of the system. The relation between  $\psi'$  and  $1 - b/b_0$  is solely affected by the value of  $\alpha$ , which determines the extent of confinement and the initial distance of the vortices from each other.

For the different transition types, we see different trends. For the supercritical transition,  $\psi'$  shows a general linear change with  $1 - b/b_0$ , with an apparently  $\alpha$ -dependent slope [Figs. 10(a) and 10(b)]. However, for subcritical transitions the relation between the parameters is non-linear [Figs. 10(c) and 10(d)].

In the high  $\alpha$  channels, we can see that initially,  $\psi'$  changes rapidly as a function of the distance between the vortices. As the vortices approach each other, there is a change in slope and  $\psi'$  increases more moderately while the distance between the vortices decreases rapidly. We interpret these two regimes as corresponding to the diffusive and convective stages of the merging and splitting processes. The general linear relation between  $\psi'$  and  $1 - b/b_0$  for low  $\alpha$  channels suggests the absence of one of the stages in merging and splitting in these more confined cases. Since the vortices only move through a relatively short distance in these low  $\alpha$

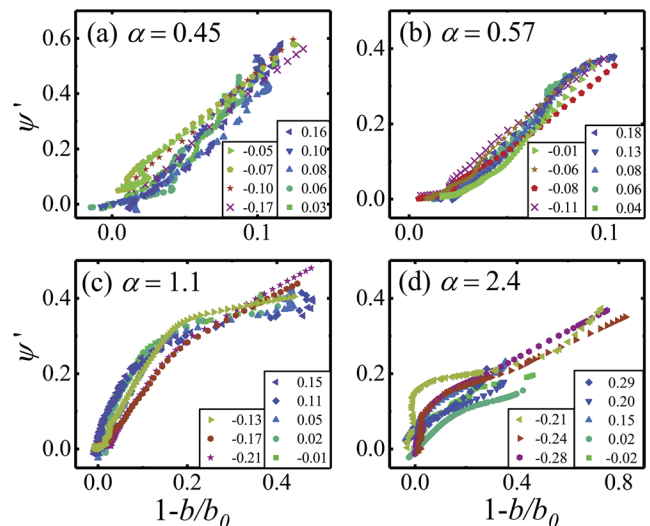


**FIG. 10.** Relation between the order parameter  $\psi'$  and the distance between merging Dean vortices  $b/b_0$ . The data plots show both increasing and decreasing  $Re$  steps experiments,  $\varepsilon_f$  is indicated in the legend. Supercritical transition (a)  $\alpha = 0.45$  and (b)  $\alpha = 0.57$ . Subcritical transition (c)  $\alpha = 1.1$  and (d)  $\alpha = 2.4$ .

cases, we conclude that the confinement results in a dominant diffusive stage and the absence of an observable convective stage.

#### IV. CONCLUSIONS

In this study, we have examined the vortex dynamics associated with a symmetry breaking flow instability that occurs beyond a critical Reynolds number in a 4-way intersecting flow. At low  $Re$ , the flow in the cross section of the intersecting region is symmetric and composed of four cells of Dean vortices. As  $Re$  is increased beyond the onset of bifurcation, one pair of diagonally opposed Dean vortices intensifies and begins to approach each other, ultimately merging to form a single vortex located on the channel centerline. By a subsequent reduction of  $Re$ , the opposite process can be induced in which a single vortex splits into two co-rotating vortices that migrate away from each other. While vortex merging has been studied extensively, the process of vortex splitting is much more challenging to induce and study. Here, by careful manipulation of the imposed Reynolds numbers in quasistatic and dynamic experiments, we are able to easily induce both the merging and splitting processes while keeping the system under a well-controlled constant steady flow. Furthermore, we can arrest the dynamics at any desired stage, permitting a detailed study of the complex flow fields and vortex interactions.

Our dynamic experiments show that the process of merging and splitting is exponential with a rate  $R_0$  that depends linearly on the imposed Reynolds number and also depends on whether the vortices are merging or separating. By changing the aspect ratio ( $\alpha$ ) of the channels leading to and from the intersection, we vary the degree of confinement of the four Dean vortices in the symmetric flow state, which has a significant effect on the rates of vortex merging and splitting. For channels with lower values of  $\alpha$ , the Dean vortices are tightly confined within quadrants of the channel cross section. This results in a relatively slow rate of vortex merging compared with splitting and reversibility of the flow transition. By contrast, for channels with higher  $\alpha$ , the Dean vortices are relatively widely spaced and unconfined. In this case, we find a faster rate of merging than of splitting. The change in the relative rates of vortex merging and splitting as  $\alpha$  is varied provides a rationalization for the emergence of hysteresis in the symmetry breaking transition at higher values of  $\alpha$ .<sup>13</sup>

The symmetry breaking and the vorticity dynamics are intimately linked, and our order parameter  $\psi$  that describes the degree of flow asymmetry is shown to depend only on the separation between Dean vortices  $b$ , independent of  $Re$  or the history of the system. The relation between  $\psi$  and  $b$  is linear for low  $\alpha$  channels (supercritical transitions, for which only a slow diffusive merging and splitting are observed) but is non-linear for the more complicated hysteretic subcritical transitions in higher  $\alpha$  channels (for which both slow diffusive and fast convective stages are seen).

Our results are clearly relevant to understanding and predicting flow transitions associated with the merging and

splitting of vortices in confined environments such as pipe flows, microfluidics, and biological flows within veins and arteries. Our discoveries may also benefit the understanding of vortex dynamics in general, particularly, with regard to the turbulent energy cascade and the prediction of vortex behavior and interactions in geophysical flows.

#### SUPPLEMENTARY MATERIAL

The [supplementary material](#) provides details of the parameters obtained from fitting the dynamic form of the Landau model to the time-resolved experimental data. We show how the fitting parameters scale with the imposed control conditions and compare these scalings with those from the existing literature on flow transitions near tricritical points.

#### ACKNOWLEDGMENTS

We gratefully acknowledge the support of the Okinawa Institute of Science and Technology Graduate University, with subsidy funding from the Cabinet Office, Government of Japan, and we also acknowledge funding from the Japan Society for the Promotion of Science (Grant Nos. 17K06173, 17J00412, 18K03958, and 18H01135). We are grateful to Mr. Kazumi Toda-Peters (Micro/Bio/Nanofluidics Unit, OIST) for help with device fabrication using LightFab.

#### REFERENCES

- 1 C. Pasquero, A. Provenzale, and J. B. Weiss, "Vortex statistics from Eulerian and Lagrangian time series," *Phys. Rev. Lett.* **89**, 284501 (2002).
- 2 D. Peters, P. Vargin, and H. Körnich, "A study of the zonally asymmetric tropospheric forcing of the austral vortex splitting during September 2002," *Tellus A* **59**, 384–394 (2007).
- 3 A. Simmons, M. Hortal, G. Kelly, A. McNally, A. Untch, and S. Uppala, "ECMWF analyses and forecasts of stratospheric winter polar vortex breakup: September 2002 in the southern hemisphere and related events," *J. Atmos. Sci.* **62**, 668–689 (2005).
- 4 A. O'Neill, C. L. Oatley, A. J. Charlton-Perez, D. M. Mitchell, and T. Jung, "Vortex splitting on a planetary scale in the stratosphere by cyclogenesis on a subplanetary scale in the troposphere," *Q. J. R. Meteorol. Soc.* **143**, 691–705 (2017).
- 5 P. R. Spalart, "Airplane trailing vortices," *Annu. Rev. Fluid Mech.* **30**, 107–138 (1998).
- 6 A. L. Chen, J. D. Jacob, and Ö. Savaş, "Dynamics of corotating vortex pairs in the wakes of flapped airfoils," *J. Fluid Mech.* **382**, 155–193 (1999).
- 7 D. Lentink, F. T. Muijres, F. J. Donker-Duyvis, and J. L. van Leeuwen, "Vortex-wake interactions of a flapping foil that models animal swimming and flight," *J. Exp. Biol.* **211**, 267–273 (2008).
- 8 A. Fani, S. Camarri, and M. V. Salvetti, "Investigation of the steady engulfment regime in a three-dimensional T-mixer," *Phys. Fluids* **25**, 064102 (2013).
- 9 D. Vigolo, S. Radl, and H. A. Stone, "Unexpected trapping of particles at a T-junction," *Proc. Natl. Acad. Sci. U. S. A.* **111**, 4770–4775 (2014).
- 10 J. T. Ault, K. K. Chen, and H. A. Stone, "Downstream decay of fully developed Dean flow," *J. Fluid Mech.* **777**, 219–244 (2015).
- 11 K. K. Chen, C. W. Rowley, and H. A. Stone, "Vortex dynamics in a pipe T-junction: Recirculation and sensitivity," *Phys. Fluids* **27**, 034107 (2015).
- 12 J. T. Ault, A. Fani, K. K. Chen, S. Shin, F. Gallaire, and H. A. Stone, "Vortex-breakdown-induced particle capture in branching junctions," *Phys. Rev. Lett.* **117**, 084501 (2016).

- <sup>13</sup>S. J. Haward, R. J. Poole, M. A. Alves, P. J. Oliveira, N. Goldenfeld, and A. Q. Shen, "Tricritical spiral vortex instability in cross-slot flow," *Phys. Rev. E* **93**, 031101 (2016).
- <sup>14</sup>N. Burshtein, K. Zografos, A. Q. Shen, R. J. Poole, and S. J. Haward, "Inertioelastic flow instability at a stagnation point," *Phys. Rev. X* **7**, 041039 (2017).
- <sup>15</sup>K. K. Chen, C. W. Rowley, and H. A. Stone, "Vortex breakdown, linear global instability and sensitivity of pipe bifurcation flows," *J. Fluid Mech.* **815**, 257–294 (2017).
- <sup>16</sup>S. T. Chan, S. J. Haward, and A. Q. Shen, "Microscopic investigation of vortex breakdown in a dividing T-junction flow," *Phys. Rev. Fluids* **3**, 072201 (2018).
- <sup>17</sup>D. Oettinger, J. T. Ault, H. A. Stone, and G. Haller, "Invisible anchors trap particles in branching junctions," *Phys. Rev. Lett.* **121**, 054502 (2018).
- <sup>18</sup>E. Sarid, C. Teodorescu, P. S. Marcus, and J. Fajans, "Breaking of rotational symmetry in cylindrically bounded 2D electron plasmas and 2D fluids," *Phys. Rev. Lett.* **93**, 215002 (2004).
- <sup>19</sup>A. J. Cerfon, "Vortex dynamics and shear-layer instability in high-intensity cyclotrons," *Phys. Rev. Lett.* **116**, 174801 (2016).
- <sup>20</sup>K. S. Fine, C. F. Driscoll, J. H. Malmberg, and T. B. Mitchell, "Measurements of symmetric vortex merger," *Phys. Rev. Lett.* **67**, 588 (1991).
- <sup>21</sup>M. T. Reeves, T. P. Billam, B. P. Anderson, and A. S. Bradley, "Identifying a superfluid Reynolds number via dynamical similarity," *Phys. Rev. Lett.* **114**, 155302 (2015).
- <sup>22</sup>W. J. Kwon, J. H. Kim, S. W. Seo, and Y. Shin, "Observation of von Kármán vortex street in an atomic superfluid gas," *Phys. Rev. Lett.* **117**, 245301 (2016).
- <sup>23</sup>P. Holmes, J. L. Lumley, G. Berkooz, and C. W. Rowley, *Turbulence, Coherent Structures, Dynamical Systems and Symmetry* (Cambridge University Press, 2012).
- <sup>24</sup>L. Biferale, F. Bonaccorso, I. M. Mazzitelli, M. A. T. van Hinsberg, A. S. Lanotte, S. Musacchio, P. Perlekar, and F. Toschi, "Coherent structures and extreme events in rotating multiphase turbulent flows," *Phys. Rev. X* **6**, 041036 (2016).
- <sup>25</sup>J. C. McWilliams, "The vortices of two-dimensional turbulence," *J. Fluid Mech.* **219**, 361–385 (1990).
- <sup>26</sup>J. Jimenez, H. K. Moffatt, and C. Vasco, "The structure of the vortices in freely decaying two-dimensional turbulence," *J. Fluid Mech.* **313**, 209–222 (1996).
- <sup>27</sup>R. Benzi, M. Colella, M. Briscolini, and P. Santangelo, "A simple point vortex model for two-dimensional decaying turbulence," *Phys. Fluids* **4**, 1036–1039 (1992).
- <sup>28</sup>L. K. Brandt and K. K. Nomura, "The physics of vortex merger and the effects of ambient stable stratification," *J. Fluid Mech.* **592**, 413–446 (2007).
- <sup>29</sup>C. Cerretelli and C. H. K. Williamson, "The physical mechanism for vortex merging," *J. Fluid Mech.* **475**, 41–77 (2003).
- <sup>30</sup>P. Meunier, S. Le Dizès, and T. Leweke, "Physics of vortex merging," *C. R. Phys.* **6**, 431–450 (2005).
- <sup>31</sup>C. Jossierand and M. Rossi, "The merging of two co-rotating vortices: A numerical study," *Eur. J. Mech.: B/Fluids* **26**, 779–794 (2007).
- <sup>32</sup>M. V. Melander, N. J. Zabusky, and J. C. McWilliams, "Symmetric vortex merger in two dimensions: Causes and conditions," *J. Fluid Mech.* **195**, 303–340 (1988).
- <sup>33</sup>I. M. Lansky, T. M. O'Neil, and D. A. Schecter, "A theory of vortex merger," *Phys. Rev. Lett.* **79**, 1479 (1997).
- <sup>34</sup>D. G. Dritschel, "A general theory for two-dimensional vortex interactions," *J. Fluid Mech.* **293**, 269–303 (1995).
- <sup>35</sup>P. G. Saffman and R. Szeto, "Equilibrium shapes of a pair of equal uniform vortices," *Phys. Fluids* **23**, 2339–2342 (1980).
- <sup>36</sup>E. A. Overman and N. J. Zabusky, "Evolution and merger of isolated vortex structures," *Phys. Fluids* **25**, 1297–1305 (1982).
- <sup>37</sup>J. Jeong and F. Hussain, "On the identification of a vortex," *J. Fluid Mech.* **285**, 69–94 (1995).
- <sup>38</sup>T. Günther and H. Theisel, "Hyper-objective vortices," *IEEE Trans. Visualization Comput. Graphics* (in press).
- <sup>39</sup>T. Leweke, S. Le Dizès, and C. H. K. Williamson, "Dynamics and instabilities of vortex pairs," *Annu. Rev. Fluid Mech.* **48**, 507–541 (2016).
- <sup>40</sup>E. J. Hopfinger and G. J. F. V. Heijst, "Vortices in rotating fluids," *Annu. Rev. Fluid Mech.* **25**, 241–289 (1993).
- <sup>41</sup>P. Freymuth, W. Bank, and M. Palmer, "First experimental evidence of vortex splitting," *Phys. Fluids* **27**, 1045–1046 (1984).
- <sup>42</sup>P. Freymuth, W. Bank, and M. Palmer, "Further experimental evidence of vortex splitting," *J. Fluid Mech.* **152**, 289–299 (1985).
- <sup>43</sup>Y. Guo and W. H. Finlay, "Splitting, merging and wavelength selection of vortices in curved and/or rotating channel flow due to Eckhaus instability," *J. Fluid Mech.* **228**, 661–691 (1991).
- <sup>44</sup>P. M. Ligrani, J. E. Longest, M. R. Kendall, and W. A. Fields, "Splitting, merging and spanwise wavenumber selection of Dean vortex pairs," *Exp. Fluids* **18**, 41–58 (1994).
- <sup>45</sup>O. S. Kerr and J. W. Dold, "Periodic steady vortices in a stagnation-point flow," *J. Fluid Mech.* **276**, 307–325 (1994).
- <sup>46</sup>J. M. Burgers, "A mathematical model illustrating the theory of turbulence," *Adv. Appl. Mech.* **1**, 171–199 (1948).
- <sup>47</sup>S. Fujiwhara, "The natural tendency towards symmetry of motion and its application as a principle in meteorology," *Q. J. R. Meteorol. Soc.* **47**, 287–292 (1921).
- <sup>48</sup>T. Günther and H. Theisel, "The state of the art in vortex extraction," *Comput. Graphics Forum* **37**, 149 (2018).
- <sup>49</sup>S. Tang and N. Aubry, "On the symmetry breaking instability leading to vortex shedding," *Phys. Fluids* **9**, 2550–2561 (1997).
- <sup>50</sup>J. Gottmann, M. Hermans, and J. Ortmann, "Digital photonic production of micro structures in glass by in-volume selective laser-induced etching using a high speed micro scanner," *Phys. Procedia* **39**, 534–541 (2012).
- <sup>51</sup>N. Burshtein, S. T. Chan, K. Toda-Peters, A. Q. Shen, and S. J. Haward, "3D-printed glass microfluidics for fluid dynamics and rheology," *Curr. Opin. Colloid Interface Sci.* **43**, 1 (2019).
- <sup>52</sup>G. Meineke, M. Hermans, J. Klos, A. Lenenbach, and R. Noll, "A microfluidic opto-caloric switch for sorting of particles by using 3D-hydrodynamic focusing based on SLE fabrication capabilities," *Lab Chip* **16**, 820–828 (2016).
- <sup>53</sup>C. D. Meinhart, S. T. Wereley, and M. H. B. Gray, "Volume illumination for two-dimensional particle image velocimetry," *Meas. Sci. Technol.* **11**, 809–814 (2000).
- <sup>54</sup>S. T. Wereley and C. D. Meinhart, "Micron-resolution particle image velocimetry," in *Microscale Diagnostic Techniques*, edited by K. S. Breuer (Springer-Verlag, Heidelberg, 2005), pp. 51–112.
- <sup>55</sup>A. Aitta, G. Ahlers, and D. S. Cannell, "Tricritical phenomena in rotating Couette-Taylor flow," *Phys. Rev. Lett.* **54**, 673–676 (1985).
- <sup>56</sup>A. Aitta, "Quantitative Landau model for bifurcations near a tricritical point in Couette-Taylor flow," *Phys. Rev. A* **34**, 2086–2092 (1986).
- <sup>57</sup>P. Meunier and T. Leweke, "Three-dimensional instability during vortex merging," *Phys. Fluids* **13**, 2747–2750 (2001).
- <sup>58</sup>P. Meunier, U. Ehrenstein, T. Leweke, and M. Rossi, "A merging criterion for two-dimensional co-rotating vortices," *Phys. Fluids* **14**, 2757–2766 (2002).
- <sup>59</sup>L. K. Brandt and K. K. Nomura, "The physics of vortex merger: Further insight," *Phys. Fluids* **18**, 051701 (2006).
- <sup>60</sup>R. V. Swaminathan, S. Ravichandran, P. Perlekar, and R. Govindarajan, "Dynamics of circular arrangements of vorticity in two dimensions," *Phys. Rev. E* **94**, 013105 (2016).
- <sup>61</sup>D. W. Moore and P. G. Saffman, "Structure of a line vortex in an imposed strain," *Aircraft Wake Turbulence and its Detection* (Springer, 1971), pp. 339–354.
- <sup>62</sup>P. G. Saffman and G. R. Baker, "Vortex interactions," *Annu. Rev. Fluid Mech.* **11**, 95–121 (1979).
- <sup>63</sup>J. P. Christiansen and N. J. Zabusky, "Instability, coalescence and fission of finite-area vortex structures," *J. Fluid Mech.* **61**, 219–243 (1973).

- <sup>64</sup>J. P. Gollub and M. H. Freilich, "Optical heterodyne test of perturbation expansions for the Taylor instability," *Phys. Fluids* **19**, 618–626 (1976).
- <sup>65</sup>A. Aitta, "Dynamics near a tricritical point in Couette–Taylor flow," *Phys. Rev. Lett.* **62**, 2116–2119 (1989).
- <sup>66</sup>P. J. S. A. Ferreira de Sousa and J. C. F. Pereira, "Laminar co-rotating Batchelor vortex merging," *Theor. Comput. Fluid Dyn.* **23**, 1–14 (2009).
- <sup>67</sup>S. Le Dizes and A. Verga, "Viscous interactions of two co-rotating vortices before merging," *J. Fluid Mech.* **467**, 389–410 (2002).
- <sup>68</sup>O. Agullo and A. D. Verga, "Exact two vortices solution of Navier–Stokes equations," *Phys. Rev. Lett.* **78**, 2361–2364 (1997).
- <sup>69</sup>T. H. Havelock, "The stability of motion of rectilinear vortices in ring formation," *Philos. Mag.* **11**, 617–633 (1931).
- <sup>70</sup>T. B. Mitchell, C. F. Driscoll, and K. S. Fine, "Experiments on stability of equilibria of two vortices in a cylindrical trap," *Phys. Rev. Lett.* **71**, 1371 (1993).
- <sup>71</sup>T. B. Mitchell and C. F. Driscoll, "Electron vortex orbits and merger," *Phys. Fluids* **8**, 1828–1841 (1996).